INTEGRATED CONTROL OF INDIVIDUAL SCALARS TO REGULATE PROFILES AND IMPROVE MHD STABILITY IN TOKAMAKS

A. PAJARES[1], E. SCHUSTER[1], A. WELANDER[2], J. BARR[2], N. EIDIETIS[2], K. THOME[2], D. HUMPHREYS[2]
[1]Lehigh University, Bethlehem, Pennsylvania 18015, USA
[2]General Atomics, San Diego, California 92121, USA
Email: andres.pajares@lehigh.edu

Abstract

Simulations using the Control-Oriented Transport SIMulator (COTSIM) and DIII-D experiments have been carried out to demonstrate the performance of a novel control architecture for simultaneous regulation of individual-scalar magnitudes. The individual scalars considered in this work include kinetic variables, such as the thermal stored energy (W) or bulk toroidal rotation (Ω_ϕ), and magnetic variables such as the safety factor profile (q) at different spatial locations. Separate control algorithms have been designed independently for each of these individual variables that use robust, nonlinear control techniques. In addition, the individual-scalar controllers have been integrated with NTM suppression algorithms, supervisory components, and an actuator manager, both within COTSIM and in the DIII-D Plasma Control System (PCS), in order to add functionalities to the control architecture and increase its level of integration. Initial simulations using COTSIM suggested that the plasma performance and its MHD stability may be improved under integrated feedback. These simulation results show good qualitative agreement with DIII-D experimental results in the steady-state high-q_{min} scenario. By means of individual-scalar feedback-control techniques in conjunction with pre-emptive and/or catch-and-subdue NTM suppression techniques, the confinement deterioration caused by NTMs in these scenarios can be significantly ameliorated.

1. INTRODUCTION

In the context of developing the necessary integrated-control architectures for present devices and future burning-plasma tokamaks, a robust, nonlinear, model-based control scheme has been designed and successfully tested in one-dimensional (1D) nonlinear simulations and DIII-D experiments. The scheme integrates four different components: (i) individual controllers [1] for the plasma thermal energy, W, bulk toroidal rotation, Ω_ϕ, and safety factor at different spatial locations (central safety factor, q_0, and edge safety factor, q_e), (ii) controllers for NTM suppression that use catch-and-subdue techniques [2] and pre-emptive stabilization [3], (iii) supervisory and exception handling (S&EH) algorithms (e.g., the Off-Normal Fault Response (ONFR) system [4] in DIII-D), and (iv) an actuator-management algorithm [5].

A simplified diagram of the control architecture is shown in Fig. 1. When accurate regulation of a whole profile becomes too difficult due to controllability issues, regulating either the value of the profile at particular spatial locations or a spatial average of the profile may be a more attainable goal. This motivates the development of controllers for simultaneous regulation of multiple individual scalars [1]. The individual-scalar controllers have been synthesized separately of each other using Lyapunov theory and Lyapunov redesign techniques [6], providing a nonlinear, robust control design. In addition, NTM controllers have been developed independently of the individual-scalar controllers [2, 3]. It is considered that the available actuators for individual-scalar control and NTM suppression are the ohmic coil, neutral beam injectors (NBIs), and electron-cyclotron (EC) launchers (gyrotrons), so that the controllable inputs to the tokamak-plasma system are the total plasma current, I_p, NBI powers, $P_{NBI,i}$ (i = 1, ..., N_{NBI}, where N_{NBI} is the total number of NBI clusters[1]), and EC powers and poloidal-mirror angles, $P_{EC,j}$ and $\phi_{EC,j}$, respectively (j = 1, ..., N_{EC}, where N_{EC} is the total number of EC clusters). The individual-scalar and NTM controllers compute higher-level individual actuation requests that are functions of I_p, $P_{NBI,i}$, $P_{EC,j}$, and $\phi_{EC,j}$, such as, for example, the total injected power necessary for W control, the NBI torque required for Ω_ϕ control, or the localized current deposition desired for q control and/or NTM suppression. Such higher-level actuation requests are received by the actuator-management algorithm, together with the actuator limits and availability (i.e., maximum/minimum physical-saturation limits and actuator failure flags). Moreover, the actuator manager takes into account the control priorities determined by S&EH algorithms, which use the plasma state to determine such priorities. With this information, the actuator manager determines the actuator requests (i.e., the controllable inputs, I_p, $P_{NBI,i}$, $P_{EC,j}$, and $\phi_{EC,j}$) that best achieve the actuation requests by solving a real-time optimization problem.

This paper is organized as follows. The models utilized for control synthesis are summarized in Section 2. The components of the control architecture are described in Section 3. Simulations results using COTSIM are included in Section 4. Some preliminary DIII-D experimental results are presented in Section 5. Finally, a conclusion and possible future work are stated in Section 6.

[1]In this work, a cluster is considered as a group of actuators whose power is regulated as a single controllable input.

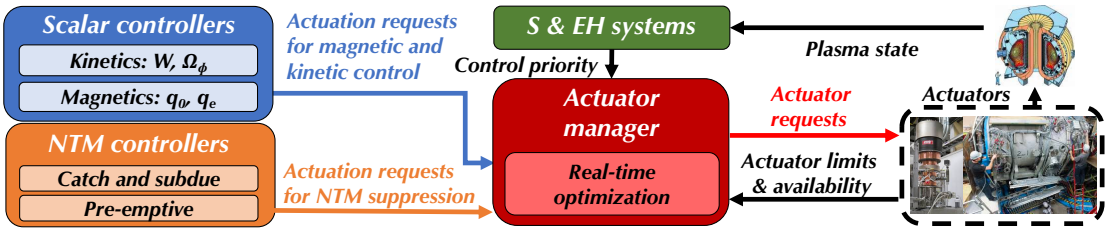

Figure 1: *Schematic of the integrated-control architecture for individual-scalar control + NTM suppression.*

2. PLASMA-TRANSPORT MODELS FOR CONTROL SYNTHESIS

2.1. Magnetic Diffusion Modeling

In this section, it is assumed that the plasma is under ideal MHD equilibrium conditions, so the magnetic-flux surfaces are nested around the magnetic axis (see Fig. 2). If toroidal symmetry is also assumed, a single spatial coordinate can be used to describe the plasma geometry. The spatial coordinate employed in this work is the mean-effective minor radius, $\rho \triangleq \sqrt{\Phi/(\pi B_{\phi,0})}$, where $B_{\phi,0}$ is the vacuum field at the geometric axis, and Φ is the toroidal flux, which at a point P is defined as $\Phi \triangleq \int_{S_\phi} \vec{B}_\phi \cdot d\vec{S}_\phi$, where B_ϕ is the toroidal component of the magnetic field, and S_ϕ is the poloidal surface whose boundary encloses the corresponding magnetic-flux surface. Similarly, the poloidal flux Ψ is defined at a point P as $\Psi \triangleq \int_{S_\theta} \vec{B}_\theta \cdot d\vec{S}_\theta$, where B_θ is the poloidal component of the magnetic field, and S_θ is the surface whose boundary is the ring that passes by P and is perpendicular to the z axis.

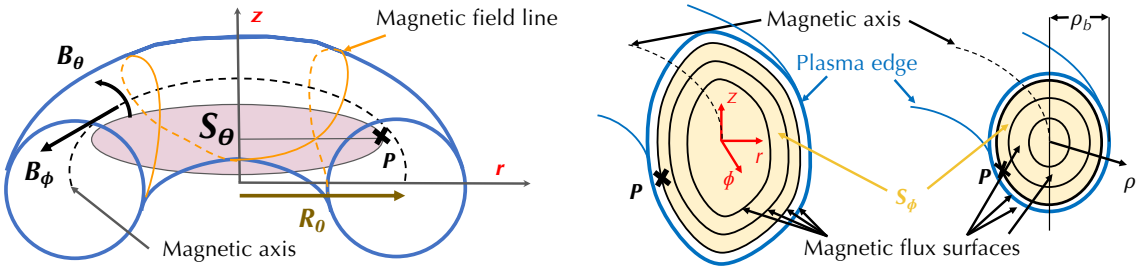

Figure 2: *Magnetic configuration in a tokamak under the assumption of ideal MHD equilibrium and toroidal symmetry. A single spatial coordinate (ρ) is employed to characterize the plasma geometry, instead of a 3D set of coordinates (r-z-ϕ).*

The basic equation to model the dynamics of the magnetic plasma variables in this work is the magnetic diffusion equation (MDE) [7] which, together with its boundary conditions, is given by

$$\frac{\partial \psi}{\partial t} = \frac{\eta}{\mu_0 \rho_b^2 \hat{F}^2} \frac{1}{\hat{\rho}} \frac{\partial}{\partial \hat{\rho}} \left(\hat{\rho} \hat{F} \hat{G} \hat{H} \frac{\partial \psi}{\partial \hat{\rho}} \right) + R_0 \hat{H} \eta \left(\sum_{i=1}^{i=N_{NBI}} j_{NBI,i} + \sum_{j=1}^{j=N_{EC}} j_{EC,j} + j_{BS} \right), \quad \left. \frac{\partial \psi}{\partial \hat{\rho}} \right|_{\hat{\rho}=0} = 0, \quad \left. \frac{\partial \psi}{\partial \hat{\rho}} \right|_{\hat{\rho}=1} = -k_{I_p} I_p, \quad (1)$$

where μ_0 is the vacuum permeability, $\psi \triangleq \Psi/(2\pi)$ is the poloidal stream function, t is the time, $\hat{\rho} \triangleq \rho/\rho_b$ (ρ_b is the value of ρ at the last-closed magnetic-flux surface), η is the plasma resistivity, R_0 is the major radius, $j_{NBI,i}$ is the current density deposited by the i-th NBI cluster, $j_{EC,j}$ is the current density deposited by the j-th EC cluster, j_{BS} is the bootstrap current-density, k_{I_p} is a model parameter, and $\hat{F}$, $\hat{G}$, and $\hat{H}$ are geometric factors of the plasma equilibrium. Physics-based, control-oriented models [8] are used for η, $j_{NBI,i}$, $j_{EC,j}$, and j_{BS},

$$\eta = \frac{k_{sp}}{T_e^{3/2}}, \quad j_{NBI,i} = j_{NBI,i}^{dep} \frac{\sqrt{T_e}}{n_e} P_{NBI,i}, \quad j_{EC,j} = j_{EC,j}^{dep}\left(\phi_{EC,j}\right) \frac{T_e}{n_e} P_{EC,j}, \quad j_{BS} = \frac{R_0}{\hat{F}} \left(\frac{\partial \psi}{\partial \hat{\rho}} \right)^{-1} \left[\mathcal{L}_1 T_e \frac{\partial n_e}{\partial \hat{\rho}} + \mathcal{L}_2 n_e \frac{\partial T_e}{\partial \hat{\rho}} \right], \quad (2)$$

where k_{sp} and $j_{NBI,i}^{dep}$ are constant model profiles, $j_{EC,j}^{dep}$ are model profiles that depend on $\phi_{EC,j}$, T_e and n_e are the electron temperature and density, respectively, and $\mathcal{L}_1$ and $\mathcal{L}_2$ are geometric factors.

2.2. Electron Particle and Heat Transport Modeling

The evolutions of n_e and T_e are modeled as

$$n_e = n_e^{prof} \bar{n}_e + \delta_{n_e}, \quad T_e = T_e^{prof} I_p \sqrt{P_{tot}} \bar{n}_e^{-1} + \delta_{T_e}, \quad (3)$$

where n_e^{prof} and T_e^{prof} are model profiles, $\bar{n}_e$ is the line-average electron density, $P_{tot} = \sum_i P_{NBI,i} + \sum_j P_{EC,j}$ is the total injected power, and δ_{n_e} and δ_{T_e} are uncertainties that characterize inaccuracies in the modeling process (e.g., unmodeled electron particle and heat sources, unexpected changes in electron confinement, MHD activity, etc.). The uncertain variables (which are denoted by $\delta_{(\cdot)}$ in this paper) are not fully known terms in the model, but it is assumed that a bound to them can be estimated. The inclusion of model uncertainties is essential to enable a robust control design that can deal with realistic limitations in the understanding of the plasma-physics phenomena.

2.3. Edge and Central Safety-Factor Modeling

The safety factor, q, is defined as $q \triangleq -d\Phi/d\Psi = -\rho_b^2\hat{\rho}B_{\phi,0}/(\partial\psi/\partial\hat{\rho})$, where the definitions for Φ, Ψ, and ρ given in Section 2.1 have been employed. The central and edge safety factors, q_0 and q_e, correspond to the value of q at the magnetic axis ($\hat{\rho} = 0$) and plasma edge ($\hat{\rho} = 1$), respectively. They are defined as

$$q_0 \triangleq -\left.\frac{\rho_b^2\hat{\rho}B_{\phi,0}}{\partial\psi/\partial\hat{\rho}}\right|_{\hat{\rho}=0} = -\left.\frac{\rho_b^2 B_{\phi,0}}{\partial^2\psi/\partial\hat{\rho}^2}\right|_{\hat{\rho}=0}, \quad q_e \triangleq -\frac{\rho_b^2 B_{\phi,0}}{\partial\psi/\partial\hat{\rho}|_{\hat{\rho}=1}} = \frac{\rho_b^2 B_{\phi,0}}{k_{I_p} I_p}, \tag{4}$$

where L'Hopital's rule has been applied within the definition of q_0, and the boundary condition at $\hat{\rho} = 1$ given in (1) has been employed within the definition of q_e. Dynamical models for q_0 and q_e are obtained from (1), (2), and (3), and the definitions in (4). The details are omitted in this work to simplify the exposition due to space constraints (more details are provided in [9]), but following a similar procedure as in [1] yields

$$\frac{dq_0}{dt} = q_0\lambda_\eta u_\eta + q_0^2\left(\sum_{i=1}^{N_{NBI}} \lambda_{NBI,i}u_{NBI,i} + \sum_{j=1}^{N_{EC}} \lambda_{EC,j}(\phi_{EC,j})u_{EC,j}\right) - q_0^3\lambda_{BS}u_{BS} + \delta_{q_0} \triangleq j_{q_0}, \tag{5}$$

$$\frac{dq_e}{dt} = -\frac{B_{\phi,0}\rho_b^2}{(k_{I_p} + \delta_{q_e})I_p^2}\frac{dI_p}{dt}, \tag{6}$$

where λ_η, $\lambda_{NBI,i}$ and λ_{BS} are model constants, $\lambda_{EC,j}$ are functions of $\phi_{EC,j}$, j_{q_0} is an auxiliary variable used to denote the right-hand side (RHS) of the q_0 dynamical equation, $u_{(\cdot)}$ are virtual inputs which are nonlinear functions of the physical inputs (i.e, I_p, $P_{NBI,i}$, $P_{EC,j}$, and $\bar{n}_e$), and δ_{q_0} and δ_{q_e} are uncertainties in the q_0 and q_e models, respectively.

2.4. Plasma Thermal-Energy Modeling

The plasma thermal energy is defined from n_e, T_e, and the density and temperature of the ions (denoted as $T_{i,p}$ and $n_{i,p}$, respectively, for the p-th ion species present in the plasma) as given by $W \triangleq \frac{3}{2}\int_{V_p}\left(n_eT_e + \sum_{p=1}^{p=N_{ion}} n_{i,p}T_{i,p}\right)dV_p$, where N_{ion} is the total number of ion species and V_p is the plasma volume. A 0D power balance is employed to model the dynamics of W as given by

$$\frac{dW}{dt} = -\frac{W}{\tau_E} + P_{tot} + \delta_W, \tag{7}$$

where δ_W is an uncertain term, and τ_E is the energy confinement time, which is modeled by the IPB98(y,2) scaling, $\tau_E = 0.0562H_H I_p^{0.93}B_{\phi,0}^{0.15}R_0^{1.97}\epsilon^{0.58}\bar{n}_e^{0.41}\kappa^{0.78}A_{eff}^{0.19}P_{tot}^{-0.69}$, where H_H is the so-called H factor, $\epsilon \triangleq a/R_0$ is the inverse aspect ratio, where a is the minor radius, κ is the plasma elongation, and A_{eff} is the plasma effective mass.

2.5. Bulk Toroidal-Rotation Modeling

The plasma is considered as a particle with mass m_p equal to the total plasma mass, which rotates at a distance R_0 in the ϕ direction (see Fig. 2) with velocity $R_0\Omega_\phi$. The angular momentum of the plasma is given by $L = m_p\Omega_\phi R_0^2$. Also, different contributions to the torque T are considered, i.e., $T = \sum_{i=1}^{N_{NBI}} T_{NBI,i} + T_{int}$, where $T_{NBI,i}$ is the contribution of the i-th NBI, which is modeled as $T_{NBI,i} = k_{NBI,i}P_{NBI,i}$, where $k_{NBI,i}$ are model parameters, and T_{int} is the intrinsic torque, which is modeled as $T_{int} = k_{int}W/I_p$, where k_{int} is a model parameter. The time variation of L is given by $dL/dt = T + \delta_{\Omega_\phi}$. Defining $\tau_{\Omega_\phi} \triangleq \frac{1}{m_p}\frac{dm_p}{dt}$ and using the model for T, the Ω_ϕ dynamics is described by

$$\frac{d\Omega_\phi}{dt} = -\frac{\Omega_\phi}{\tau_{\Omega_\phi}} + \frac{1}{m_pR_0^2}\left(\sum_{i=1}^{N_{NBI}} k_{NBI,i}P_{NBI,i} + k_{int}\frac{W}{I_p} + \delta_{\Omega_\phi}\right). \tag{8}$$

In equation (8), m_p and τ_{Ω_ϕ} are modeled as $m_p = m_D\frac{\bar{n}_eV_p}{N_{av}}$ and $\tau_{\Omega_\phi} = k_{\Omega_\phi}\tau_E$, where m_D is the molar mass of the plasma ions, N_{av} is Avogadro's number, and k_{Ω_ϕ} is a model parameter.

2.6. NTM Island-Width Modeling

The dynamic evolution of the NTM island-width, w, is modeled by means of the Modified Rutherford Equation (MRE). The version utilized in this work is very similar to that in [3],

$$\frac{\tau_R}{r}\frac{dw}{dt} = \Delta' r + a_2\frac{j_{BS}(\hat{\rho}_{NTM})}{j_\phi(\hat{\rho}_{NTM})}\frac{L_q}{w}\left(1 - \frac{w_{marg}^2}{3w^2} - \sum_{j=1}^{j=N_{EC}} K_{EC,j}\frac{j_{EC,j}(\hat{\rho}_j^{max})}{j_{BS}(\hat{\rho}_{NTM})}\right), \tag{9}$$

where τ_R is the island's resistive diffusion time, Δ' is the TM stability index, r is the radial location (see Fig. 2) of the island, a_2 is a geometric factor, j_{BS} and j_ϕ are the bootstrap and toroidal current densities, respectively, $\hat{\rho}_{NTM}$ is the NTM location in terms of $\hat{\rho}$, $L_q \triangleq (q/|dq/dr|)|_{\hat{\rho}_{NTM}}$ is the local magnetic-shear length, w_{marg} is the marginal island width, $\hat{\rho}_j^{max}$ is the location of the maximum of $j_{EC,j}$, and $K_{EC,j}$ are parameters that model how each ECCD

cluster affects the island growth by localized deposition. The factors $K_{EC,j}$ depend on the alignment of the ECCD cluster with the NTM island, so they vary with $|\phi_{EC,j} - \hat{\rho}_{NTM}|$. The island's resistive diffusion time is modeled as $\tau_R = \frac{\mu_0 \pi r w}{1.22\eta(\hat{\rho}_{NTM})}$, whereas $\Delta' r$ is given by

$$\Delta' r = \Delta'_0 r - \frac{a_2 L_q}{j_\phi(\hat{\rho}_{NTM})} \sum_j \frac{F_{EC,j}}{\delta^w_{EC,j}} j_{EC,j}(\hat{\rho}^{max}_j), \tag{10}$$

where $\Delta'_0 = -m/r$ is the classical TM stability index (for an NTM at $q = m/n$), $\delta^w_{EC,j}$ characterize the width of the ECCD deposition, and $F_{EC,j}$ are functions that depend on $|\phi_{EC,j} - \hat{\rho}_{NTM}|$. The marginal island width is estimated as $w_{marg} = 2\sqrt{\epsilon}\rho_{i,\theta}$, where $\rho_{i,\theta} = 2.043 \times 10^{-4} \sqrt{T_D(\hat{\rho}_{NTM})/B_\theta(\hat{\rho}_{NTM})}$), and T_D is the deuterium temperature.

2.7. Control-Synthesis Model Summary and Control Goal

The control-synthesis model can be written as $\dot{x} = f(x, u, \delta, t)$, where $x = [q_0, q_e, W, \Omega_\phi, w]^T$ is the state vector, $u = [I_p, P_{NBI,1}, ..., P_{NBI,N_{NBI}}, P_{EC,1}, ..., P_{EC,N_{EC}}, \phi_{EC,1}, ..., \phi_{EC,N_{EC}}]^T$ is the vector of controllable inputs, $\delta = [\delta_{q_0}, \delta_{q_e}, \delta_W, \delta_{\Omega_\phi}]^T$ is the vector of uncertainties, and $f = [f_{q_0}, f_{q_e}, f_W, f_{\Omega_\phi}, f_w]^T$, where the functions f_{q_0}, f_{q_e}, f_W, f_{Ω_ϕ}, and f_w are given by the RHS of (5), (6), (7), (8), and (9), respectively. The goal of the control scheme is to regulate x around a target $\bar{x}$ for all values $\delta \in [-\delta^{max}, \delta^{max}]$ (where δ^{max} is the maximum attainable value of δ) by means of u, where $u \in [u_{min}, u_{max}]$, and u_{min} and u_{max} are the minimum and maximum saturation limits for u.

3. CONTROL ARCHITECTURE

3.1. Controllers for Individual Scalars (q_0, q_e, W, Ω_ϕ, and w)

Controllers for q_0, q_e, W, and Ω_ϕ are synthesized in a similar way as in [1] . These controllers calculate the necessary values for j_{q_0}, I_p, P_{tot}, and T_{NBI} (denoted by $j^{req}_{q_0}$, I^{req}_p, P^{req}_{tot}, and T^{req}_{NBI}, respectively, and referred to as "actuation requests") to control q_0, q_e, W, and Ω_ϕ, respectively, around the targets $\bar{q}_0$, $\bar{q}_e$, $\bar{W}$, and $\bar{\Omega}_\phi$. It must be noted that the controllable input u is not uniquely determined by these controllers alone. Instead, the actuation requests are sent to the actuator manager (see Section 3.3), which is the scheme's component that calculates u.
In addition, control algorithms to specify $\phi_{EC,j}$ were designed in [2, 3] that employ pre-emptive stabilization and catch-and-subdue (C&S) techniques. With pre-emptive stabilization, the ECCD is always turned on and applied at particular rational surfaces that are prone to NTMs, so that the magnetic islands do not develop. On the other hand, with C&S techniques, the ECCD remains off until an NTM is detected. Then, the EC power is turned on, and $\phi_{EC,j}$ are steered toward the spatial location of the NTM for its suppression. When sufficient shrinkage of the magnetic island is achieved, the ECCD is turned back off. In this work, both techniques are considered. For convenience, $j^{dep}_{c\&s}$, $P_{c\&s}$, and $\phi_{c\&s}$ denote the model profile, power, and mirror angle, respectively, of the cluster employed for C&S suppression, $N_{EC,pre}$ is the total number of pre-emptive-stabilization clusters, and $j^{dep}_{EC,k}$, $P_{EC,k}$, and $\phi_{EC,k}$ ($k = 1, ..., N_{EC,pre}$) are the model profiles, powers, and mirror angles, respectively, of the pre-emptive-stabilization clusters. The total ECCD, $j_{EC,tot} \triangleq \sum_j j_{EC,j}$, has contributions from both the pre-emptive and C&S suppression clusters. Using (2), $j_{EC,tot}$ can be expressed as

$$j_{EC,tot} \triangleq \sum_j j_{EC,j} = \frac{T_e}{n_e} \left(\sum_k j^{dep}_{EC,k}(\phi_{EC,k}) P_{EC,k} + j^{dep}_{c\&s}(\phi_{c\&s}) P_{c\&s} \right). \tag{11}$$

Usually, $P_{EC,k}$ are fixed and set equal to the maximum available power, $P^{req}_{EC,k}$. Moreover, $\phi_{EC,k}$ and $\phi_{c\&s}$ are determined by a separate algorithm (e.g., [2, 3]) to aim at the rational surface(s) that are prone to NTMs (in the case of pre-emptive stabilization) or that have developed NTMs (in the case of C&S). The required poloidal-mirror angles are denoted as $\phi^{req}_{EC,k}$ and $\phi^{req}_{c\&s}$. As a result, the only variable left for real-time control is $P_{c\&s}$, for which a controller is designed using Lyapunov theory [6]. Using (10) and (11), (9) can be rewritten as

$$\frac{\tau_R}{r}\frac{dw}{dt} = \Delta'_0 r + a_2 \frac{j_{BS}}{j_\phi}\frac{L_q}{w}\left(1 - \frac{w^2_{marg}}{3w^2}\right) - \frac{a_2 L_q}{j_\phi}\left[\sum_k \left(\frac{F_{EC,k}}{\delta^w_{EC,k}} + \frac{K_{EC,k}}{w}\right) j_{EC,k}(\hat{\rho}^{max}_k) + \left(\frac{F_{c\&s}}{\delta^w_{c\&s}} + \frac{K_{c\&s}}{w}\right) j_{c\&s}(\hat{\rho}^{max}_{c\&s})\right], \tag{12}$$

where the dependence with $\hat{\rho}_{NTM}$ is dropped to simplify the notation, and all variables associated with the C&S cluster are denoted by the subindex $(\cdot)_{c\&s}$. By setting

$$j_{c\&s}(\hat{\rho}^{max}_{c\&s}) = \frac{K_P(w^2 \tau_R j_\phi)/(rL_q) + j_{BS}}{wF_{c\&s}/\delta^w_{c\&s} + K_{c\&s}}, \tag{13}$$

where $K_P > 0$ is a design parameter, (12) becomes

$$\frac{\tau_R}{r}\frac{dw}{dt} = \Delta'_0 r - \frac{\tau_R}{r} a_2 K_p w - a_2 \frac{j_{BS}}{j_\phi}\frac{L_q}{w}\frac{w^2_{marg}}{3w^2} - \frac{a_2 L_q}{j_\phi}\sum_k \left(\frac{F_{EC,k}}{\delta^w_{EC,k}} + \frac{K_{EC,k}}{w}\right) j_{EC,k}(\hat{\rho}^{max}_k). \tag{14}$$

It is assumed that $P^{req}_{EC,k}$ and $\phi^{req}_{EC,k}$ provide a stabilizing effect, so the last term in (14) is non-positive. Because

the first and third terms on the RHS of (14) are always strictly negative, dw/dt in (14) can be bounded as $\frac{dw}{dt} < -a_2 K_p w \implies w < w_0 e^{-t/\tau}$, where w_0 is the initial island width, and $\tau \triangleq 1/(a_2 K_p)$. Therefore, (14) is an exponentially stable system [6]. The control law (13) ensures that $w \to 0$ as $t \to \infty$ bounded by an exponential with characteristic time τ. The required power for C&S suppression, $P^{req}_{c\&s}$, is computed from (2), (11) and (13) as

$$P^{req}_{c\&s} = \frac{1}{j^{dep}_{c\&s}(\hat{\rho}^{max}_{c\&s})} \left[\frac{n_e(\hat{\rho}^{max}_{c\&s})}{T_e(\hat{\rho}^{max}_{c\&s})} \frac{\frac{\tau_R}{r}\frac{K_P j_\phi}{L_q} w^2 + j_{BS}}{w\frac{F_{c\&s}}{\delta^w_{c\&s}} + K_{c\&s}} - \sum_k j^{dep}_{EC,k}(\hat{\rho}^{max}_k) P_{EC,k} \right]. \tag{15}$$

Finally, the NTM controllers send their computed actuations requests (i.e., $P^{req}_{c\&s}$, $\phi^{req}_{c\&s}$, $P^{req}_{EC,k}$, and $\phi^{req}_{EC,k}$) to the actuator manager (see Section 3.3).

3.2. Supervisory and Exception Handling Systems

Supervisory and exception handling (S&EH) systems will be a critical component in future integrated PCSs. In general terms, a S&EH system receives information from the plasma state in order to decide, in real time, the priorities of the control tasks that need to be carried out for a safe and efficient tokamak operation. The Off-Normal Fault-Response (ONFR) system [4], implemented and tested within the DIII-D PCS, has some S&EH capabilities. For example, it has the capability of monitoring MHD instabilities such as NTMs. In this work, the ONFR system has been employed during DIII-D experiments to monitor the NTM development so that, in conjunction with the controllers for individual scalars + NTM suppression and an actuator manager, simultaneous control objectives can be attained. When an NTM that needs suppression is detected by ONFR, this control priority is sent to the actuator manager so that the NTM-suppression actuation requests are fulfilled as closely as possible. On the other hand, when there is no need for NTM suppression, the individual-scalar actuation requests are prioritized. This is done by modifying (in real time) the design matrices embedded in the actuator manager (see Section 3.3).

3.3. Actuator Management and Sharing

The development of actuator managers within the aforementioned integrated PCS architectures will be essential. Numerous control tasks need to be carried out, sometimes simultaneously, by a finite number of actuators. Examples include the ECCD sharing for NTM suppression and q-profile control purposes, or the NBI sharing for W and Ω_ϕ regulation. The goal of an actuator manager is to determine the controllable input u that can fulfill as many control objectives (i.e., actuation requests) as possible, while also considering actuator limits and availability, as well as other secondary objectives (e.g., minimizing the control effort). In this work, an actuator manager based on real-time optimization [5] is used. It receives the actuation requests from individual-scalar and NTM suppression controllers, information about actuation limits and availability, and information about control and actuator priorities from S&EH systems. The optimization problem that is solved in real time is given by

$$\min_{u,s} u^T R u + s^T Q s, \text{ subject to} \tag{16}$$

$$\textbf{Kinetic control constraints: } \sum P_{NBI,i} + \sum P_{EC,j} = P^{req}_{tot} + s_{P_{tot}}, \quad \sum k_{NBI,i} P_{NBI,i} = T^{req}_{NBI} + s_{T_{NBI}}, \tag{17}$$

$$\textbf{Magnetic control constraints: } I_p = I^{req}_p + s_{I_p}, \quad j_{q_0}(q_0, I_p, P_{NBI,i}, P_{EC,j}) = j^{req}_{q_0} + s_{j_{q_0}}, \tag{18}$$

$$\textbf{NTM suppression constraints: } P_{EC,j} = P^{req}_{EC,j} + s_{P_{EC,j}}, \quad \phi_{EC,j} = \phi^{req}_{EC,j} + s_{\phi_{EC,j}}, \tag{19}$$

$$\textbf{Saturation limits and actuator availability: } u \in [u_{min}, u_{max}], \tag{20}$$

where $s = [s_{P_{tot}}, s_{T_{NBI}}, s_{I_p}, s_{j_{q_0}}, s_{P_{EC,1}}, ..., s_{P_{EC,N_{EC}}}]^T$ is a vector of slack variables that characterize the fulfillment of a particular actuation request, and Q and R are matrices that determine how the different actuators and control tasks are prioritized. For example, if NTM suppression is needed as determined by a S&EH algorithm, the terms in Q related to $s_{P_{EC,k}}$ and $s_{\phi_{EC,k}}$ are much higher in order to make those slacks small and prioritize the use of ECCD for this control task. Similarly, if an actuator's control action becomes "expensive" (for instance, as a protective measure for excessive power-modulation of an NBI), the terms in R related to the particular actuator are increased.

4. ONE-DIMENSIONAL SIMULATIONS USING COTSIM

The control architecture has been tested in simulations using COTSIM. Within this 1D simulation code, transport equations for ψ, T_e, and the toroidal rotation, ω_ϕ, are employed in conjunction with physics-based models for η, Gyro-Bohm models for the electron thermal and momentum ion diffusivities, χ_e and χ_ϕ [10], as well as analytical models for the pedestal temperature and height [11]. The MRE is also evolved and coupled with the transport equations, so that the development of NTMs decreases the overall confinement levels. These models include more comprehensive plasma-dynamics than the control-synthesis models described in Section 2. This increase in model complexity represents a challenging test for the controllers' robustness against unknown dynamics.

The objective of this simulation study is to assess the control scheme's performance to regulate the individual scalars when NTMs are present in the DIII-D high-q_{min} scenario. Three NBI clusters are used: on-axis, off-axis and counter-current NBIs. Also, three ECCD sources are utilized. First, a feedforward (FF) simulation is run with the experimental inputs from shot 172538, except for $P_{EC} \triangleq \sum P_{EC,j}$, which is reduced from 3.5 MW to 1.5 MW. Also, the development of a 2/1 NTM is emulated after $t = 2.7$ s as a result of the reduced P_{EC}. No feedback (no FB) is employed in this first simulation. Second, another FF simulation is run with lower I_p (-0.2 MA compared to 172538), $P_{EC} \approx 1.5$ MW, and increased off-axis power but decreased on-axis power (+25% and -25% with respect to 172538, respectively). No NTM is emulated in this case. The evolutions for the scalars during this second simulation are set as the targets for a subsequent FF + FB simulation, i.e., $\bar{q}_0$, $\bar{q}_e$, $\bar{W}$, and $\bar{\Omega}_\phi$, respectively. Finally, a third simulation is executed in which the FB control scheme is turned on at $t = 0.9$ s to drive x toward $\bar{x}$. The FB controllers use the FF inputs from the first simulation, but they do not know anything about the inputs associated with the targets (i.e., with the inputs of the second FF simulation).

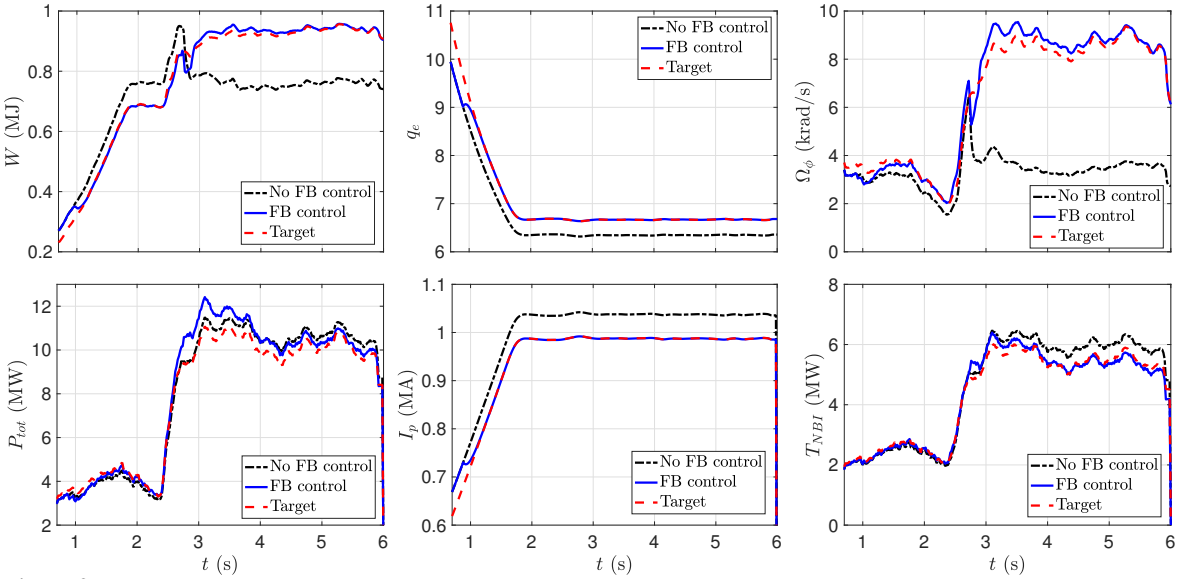

Figure 3: *Time evolutions for W, q_e, Ω_ϕ, P_{tot}, I_p, and T_{NBI} in FF (black dashed-dotted) and FF + FB (blue solid) simulations using the one-dimensional code COTSIM, together with the targets (red dashed).*

Fig. 3 shows the evolution of W, q_e, Ω_ϕ, P_{tot}, I_p, and the NBI torque $T_{NBI} \triangleq \sum_{i=1}^{N_{NBI}} T_{NBI,i}$, whereas Fig. 4 shows the evolution of q_0, P_{210} (counter-current NBI power; beamline located at toroidal angle of 210 deg), P_{150} (off-axis NBI power; beamline located at toroidal angle of 150 deg), w, $\hat{\rho}_{ECCD,j}$, $\hat{\rho}_{NTM}$, and P_{EC}. It can be seen that W decreases around $t = 2.7$ s without FB control due to the NTM development (see Fig. 3, top left), whereas using FB allows for driving W toward its target by modulating P_{tot} (see Fig. 3, bottom left). It can be seen that P_{tot} is increased in FB with respect to the target case after the NTM develops, and only converges toward the target later in the simulation. Also, q_e and Ω_ϕ are driven toward their targets in FB (see Fig. 3, top middle and right) despite temporary deviations due to the effects of the NTM. Both I_p and T_{NBI} are driven toward the target evolutions under FB (see Fig. 3, bottom middle and right), although the controllers do not have such information. On the other hand, q_0 is also successfully regulated in FB to avoid the drop caused by the NTM (see Fig. 4, top left). This is done by modulating the different NBI and EC cluster powers (see Fig. 4, top middle and right for P_{210} and P_{150}, and bottom right for P_{EC}). Although P_{tot} is increased in FB with respect to the target case after the NTM develops (possibly due to transient changes in q and χ_e), it eventually converges toward the target. On the other hand, all $\rho_{EC,j}$ are steered at $t = 2.7$ s from its initial position toward $\hat{\rho}_{NTM}$, in order to drive w to zero (see Fig. 4, bottom left and middle). Otherwise, the island grows and saturates with $w \approx 10$ cm in the no FB case.

5. EXPERIMENTAL RESULTS IN DIII-D

The control architecture has been experimentally tested in the high-q_{min} scenario in DIII-D. Fig. 5 shows the evolution of the variables related to q_e control (q_e, I_p, and $B_{\phi,0}/R_0$) and W control (W, P_{tot}, and H_H) for shots 180390 (no feedback control) and 180397 (in which the FB control scheme is turned on at $t = 2$ s). It can be observed that, despite using the same I_p evolution from the beginning of the discharge until $t = 2$ s (see Fig. 5, top middle), variations in q_e between shots 180390 and 180397 are found (see Fig. 5, top left) due to small variations in the plasma equilibrium and other relevant variables (e.g., $B_T/R_0 \propto dq_e/dt$, see Fig. 5, top right). After the FB controllers are turned on at $t = 2$ s, I_p is modified in order to drive q_e toward the desired target. It must be noted that the control-synthesis model has no real-time information about the variations in the plasma equilibrium, R_0, or B_T, demonstrating the controller's robustness against unknown plasma dynamics. Similarly, the W evolution is

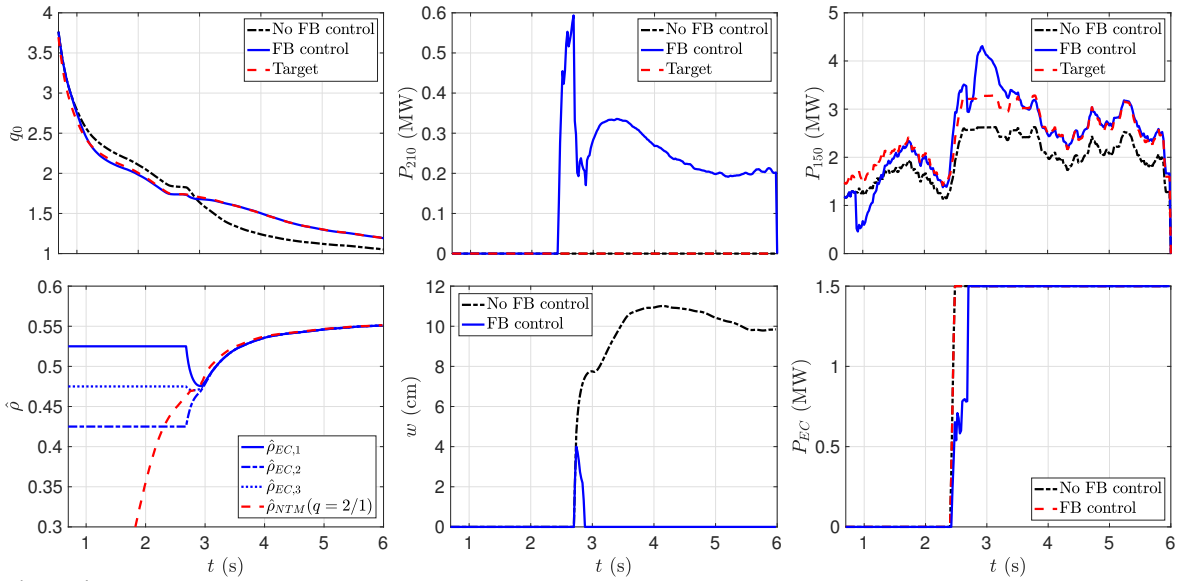

Figure 4: *Time evolutions for q_0, P_{210}, P_{150}, $\rho_{EC,j}$, $\hat{\rho}_{NTM}$, w, and P_{EC} in FF (black dashed-dotted) and FF + FB (blue solid) simulations using the one-dimensional code COTSIM, together with the target evolutions (red dashed).*

different in 180390 and 180397 before $t = 2$ s (see Fig. 5, bottom left) due to variations in P_{tot} (see Fig. 5, bottom middle) which were caused by partial failures in the 330R beam (radially-directed beamline located at toroidal angle of 330 deg). After $t = 2$ s, W is significantly reduced by the development of a 2/1 NTM in the no FB case, but P_{tot} is modulated to drive W toward the desired target under FB. Despite increasing P_{tot} substantially, H_H is improved under FB by about +30% (see Fig. 6, bottom right).

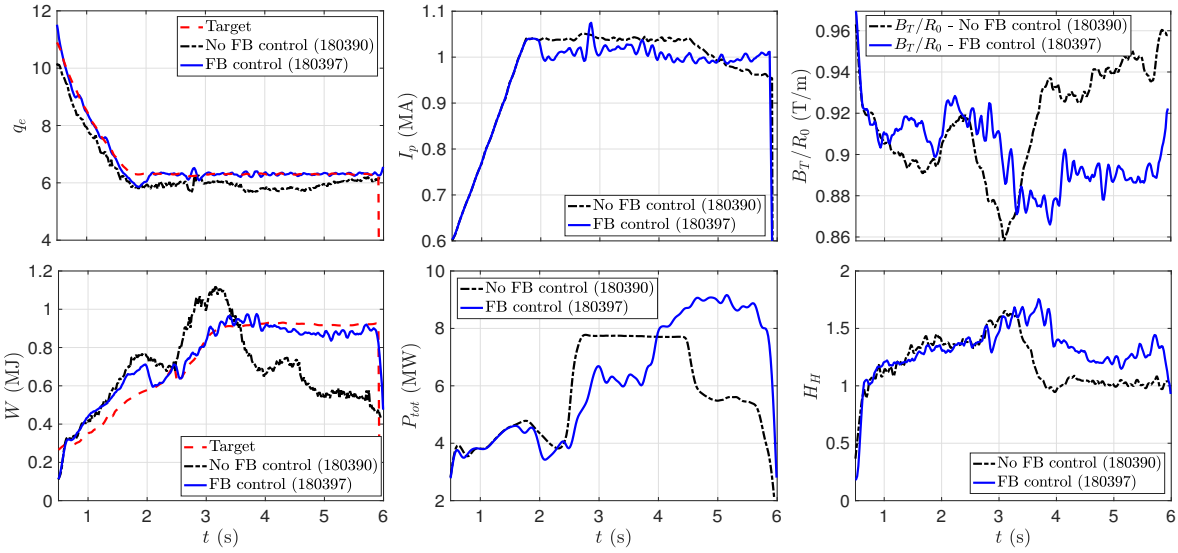

Figure 5: *Time evolutions of q_e, I_p, B_T/R_0, W, P_{tot}, and H_H in DIII-D shots 180397 (solid blue) and 180390 (black dashed-dotted), and targets for q_e and W (red dashed). Good performance under FB is observed in shot 180397, as well as better performance than in shot 180390.*

The unavailability and lack of power of different actuators limited the controllability of other individual scalars in this DIII-D experiment. First, no counter-current NBIs were available, so Ω_ϕ regulation was not possible. Moreover, the controller's performance to regulate q_0 was significantly limited by the lack of off-axis power (it was only possible to employ the 210 beamline in co-current configuration for a 2 s pulse, and after $t \approx 3.25$ s) and the development of NTMs, which could not be totally suppressed. Fig. 6 compares shot 180399 (in which q_0 was FB controlled) with 180390. When the 210 beamline is turned on at $t = 3.25$ s (see the magenta triangle in Fig. 6, top left), q_0 is driven toward its target (see Fig. 6, top left). Acceptable regulation is achieved under FB between $t \approx 3.25$ and $t \approx 3.8$ s by modulating P_{210} and P_{150} (see Fig. 6, top middle and right). For clarity purposes, the non-controlled evolution of q_0 during shot 180390 in $t \in [3.4, 3.8]$ s has not been shown. Around $t \approx 3.8$ s, a 2/1 NTM develops in the FB case (see the orange triangle in Fig. 6, top left). The associated reduction in T_e (which increases η) relaxes the q profile and makes it difficult for the controller to raise q_0 in order to reach the desired target, despite significantly increasing P_{210} and P_{150}. Still, q_0 remains closer to its target under FB. Also, the low P_{EC} (≈ 1.5 MW maximum, see Fig. 6, bottom right) and inaccurate ECCD steering under FB (see Fig. 6, bottom left) were possible reasons for not achieving higher NTM suppression (see Fig. 6, bottom middle), although a delay in its appearance and slightly reduced strength were consistently achieved (e.g., shot 180403).

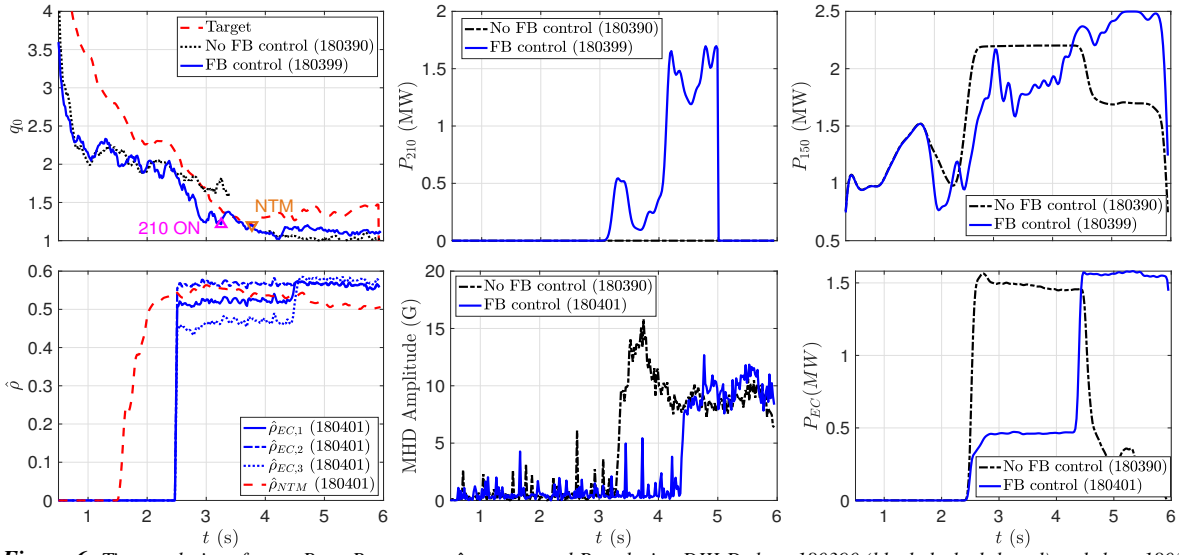

Figure 6: *Time evolutions for q_0, P_{210}, P_{150}, $\rho_{EC,j}$, $\hat{\rho}_{NTM}$, w, and P_{EC} during DIII-D shots 180390 (black dashed-dotted) and shots 180399 and 180401 (blue solid), together with the target evolutions (red dashed).*

6. CONCLUSION AND POSSIBLE FUTURE WORK

The integrated-control architecture for scalars + NTM control has shown excellent performance in 1D nonlinear simulations and promising results in experiments with limited actuation capability. Similar plasma dynamics and controller performance are observed in simulations and experiments, showing that COTSIM can be a powerful tool for control development and experimental planning. Future work may expand the individual-scalar controllers considered (e.g., adding l_i or q_{min} control), its integration with other DIII-D PCS supervisory components, and the generalization of the actuator-manager algorithm to handle a larger set of control tasks and actuators.

ACKNOWLEDGMENTS

This work was supported by the US Department of Energy under DE-SC0010661 and DE-FC02-04ER54698.

REFERENCES

[1] A. PAJARES AND E. SCHUSTER, "Integrated Robust Control of Individual Scalar Variables in Tokamaks", in *IEEE Conference on Decision and Control (CDC)*, 3233–3238 (2019)

[2] R. L. HAYE ET AL., Control of Neoclassical Tearing Modes in DIII-D, Physics of Plasmas, **9**, (2002)

[3] R. L. HAYE ET AL., Higher Stable Beta by Use of Pre-emptive ECCD on DIII-D, Nucl. Fusion, **45**, L37 (2005)

[4] N. EIDIETIS ET AL., Implementing a Finite-State Off-Normal and Fault Response System for Disruption Avoidance in Tokamaks, Nucl. Fusion, **58**, (2018)

[5] A. PAJARES AND E. SCHUSTER, "Actuator Management via Real-time Optimization for Integrated Control in Tokamaks", in *46th EPS Conference on Plasma Physics* (2019)

[6] H. Khalil, *Nonlinear Systems*, Prentice Hall, 3rd edition (2001)

[7] F. HINTON AND R. HAZELTINE, Theory of Plasma Transport in Toroidal Confinement Systems, Rev. Mod. Phys., **48**, 239 (1976)

[8] J. BARTON ET AL., "Physics-based Control-oriented Modeling of the Safety Factor Profile Dynamics in High Performance Tokamak Plasmas", in *IEEE Conference on Decision and Control (CDC)*, 4182–4187 (2013)

[9] A. PAJARES, E. SCHUSTER ET AL., Integrated Control of Individual Scalars to Regulate Profiles and Improve MHD Stability in Tokamaks, to be submitted to Nuclear Fusion (2021)

[10] M. ERBA ET AL., Validation of a New Mixed Bohm/gyro-Bohm Model for Electron and Ion Heat Transport against the ITER, Tore Supra and START Database Discharges, Nucl. Fusion, **38**, 1013 (1998)

[11] T. ONJUN ET AL., Models for the Pedestal Temperature at the Edge of H-mode Tokamak Plasmas, Phys. Plasmas, **9** (2002)